CHAPTER 4

RESULTS AND DISSCUSSION

4.1 Physical characterization of the synthesized nanostructures

XRD patterns of undoped ZnO and Sn-doped ZnO nanostructures synthesized by FSP as shown in Figure 4.1, demonstrate that the nanostructures were obtained only in wurtzite ZnO structure (JCPDS file no. 89-0510).

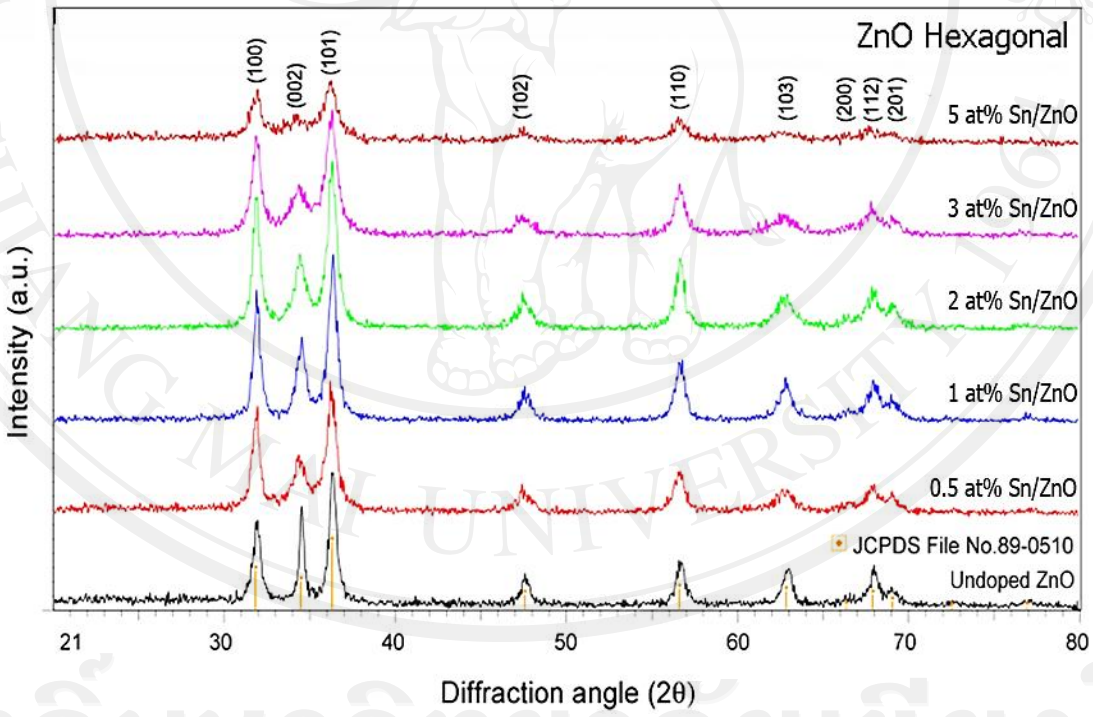

Figure 4.1 XRD patterns of undoped ZnO and Sn-doped ZnO nanostructures synthesized by FSP with different Sn concentrations

The secondary phases of Sn segregation as well as SnO_2 crystallite could not be observed. The absence of Sn related peaks could be attributed to two reasons, their

ลิขสิทธิ์มหาวิทยาลัยเชียงใหม่
Copyright© by Chiang Mai University
All rights reserved

ultra-fine dispersion on ZnO as very small clusters or very low Sn contents. Nevertheless, it can be observed that (002) peak of ZnO exhibits a clear reduction of the intensity and increase of broadness as Sn concentration increases. The crystallite sizes of the samples could find from the relationship between crystallite size and peak width at half maximum intensity, described by the Scherrer's equation:

$$\beta_k = \frac{k_S \cdot \lambda}{d_{hkl} \cdot \cos(\theta)} \tag{4.1}$$

where β_k is peak width at half maximum intensity, k_S is shape factor, λ is wavelength (usually 1.54056 Å for Cu Kα), d_{hkl} is crystallite size, and θ is peak position. The three main peaks, i.e. at (100), (002) and (101) plane, of all samples were fitted (Appendix C) and the crystallite sizes of the samples were calculated as Equation 4.1 (Figure 4.2). In Figure 4.2, the crystallite size (d_{XRD}) of (002) plane becomes smaller from 15.37 to 2.84 nm with increasing contents of Sn from 0 to 5 at% in ZnO. Moreover, the crystallite sizes in (101) planes were also slightly decreased from 13.05 to 9.10 nm following the increase of doping level from 0 to 5 at%. The decrease of grain size of ZnO with increasing Sn content is consistent with other reports by Tsay et al. [77] and Trinh et al. [85]. Their analysis of Sn-doped ZnO films prepared by the sol-gel method suggested that Sn^{4+} substituted into the Zn^{2+} site in the crystal structure causing XRD Bragg peak intensity as well as the grain size reduced. At higher Sn contents, Sn^{4+} ions (0.69 Å) [52] occupy more Zn^{2+} (0.74 Å) sites in ZnO lattice due to the similarity in their ionic radii and become the obstructers through the growth of ZnO crystallite in (002) plane during synthesis process. This can be especially true for FSP synthesis that exhibits high peak temperatures around

ลิขสิทธิ์มหาวิทยาลัยเชียงใหม่
Copyright© by Chiang Mai University
All rights reserved

1,700−2,200°C [93] depending on particular solvent, starting materials and dopants used [138], which is a driving force for generating much more substitutional point defect. Furthermore, the intensity variation of each peak by Sn dopant indicates that ZnO nanostructures grow along the direction that is considerably depending on synthesis parameters.

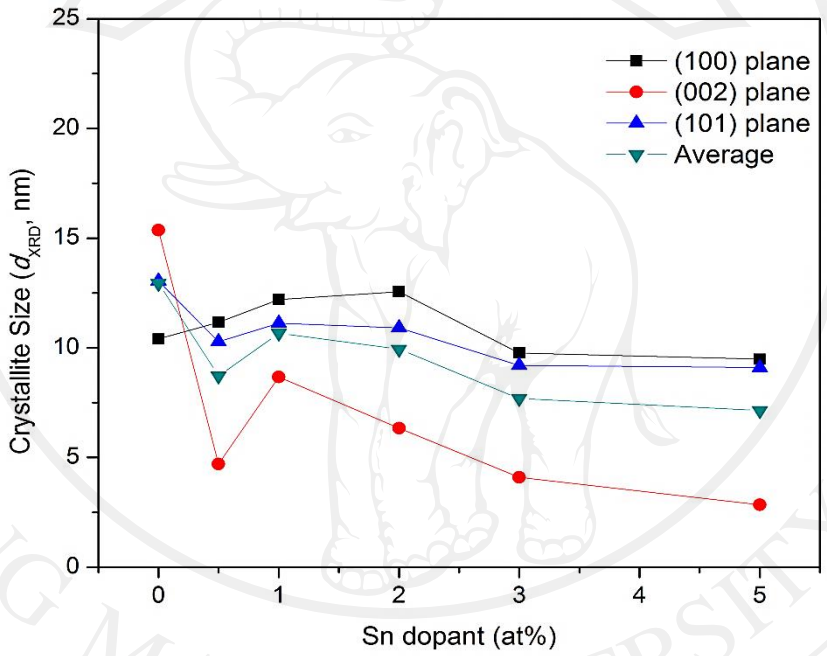

Figure 4.2 Crystallite size in (100), (002) and (101) planes, from XRD, of undoped ZnO and Sn-doped ZnO nanostructures synthesized by FSP with different Sn concentrations

A hexagonal close packed wurtzite structure of ZnO composes of stacking of planes of Zn and O atoms shown as (Figure 4.3). The (002) plane lies along *c*-axis or ⟨0001⟩ direction and in parallel to the O and Zn planes, while the (100) plane lies

ลิขสิทธิ์มหาวิทยาลัยเชียงใหม่
Copyright© by Chiang Mai University
All rights reserved

along $\langle 2110 \rangle$ direction and perpendicular to the (002) plane. The crystallite sizes in the (002) and (100) planes can basically be considered as metrics of "Diameter" (D_a) and "Length" (L), respectively (Figure 4.3). The crystal aspect ratio (L / D_a) of ZnO nanostructure morphology in rod type can be estimated by the ratio of the crystallite sizes (d_{XRD}) in the (100) and (002) planes. Figure 4.3 (a) showed the variation of XRD lattice aspect ratio with dopant concentration for the Sn-doped ZnO as calculated from the d_{XRD} measurements. The XRD lattice aspect ratio slightly decreased from 0.68 to 3.33 as the Sn dopant concentration was increased from 0 to 5 at%. These showed that Sn doping in ZnO structures with FSP method powerfully affects the morphology transform towards rod-like morphology by dramatically decreasing crystallite size in diameter (Figure 4.2).

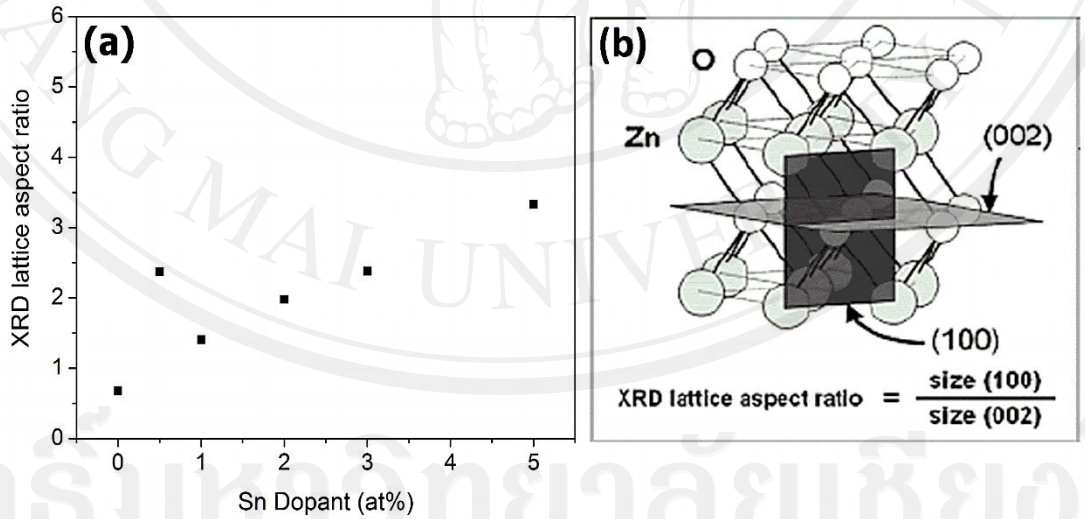

Figure 4.3 (a) The calculation of XRD lattice aspect ratio (L / D_a) using the (100) and (002) crystallite sizes of 0−5 at% Sn-doped ZnO, corresponding with (b) ZnO hexagonal-close-packed wurtzite structure

ลิขสิทธิ์มหาวิทยาลัยเชียงใหม่
Copyright© by Chiang Mai University
All rights reserved

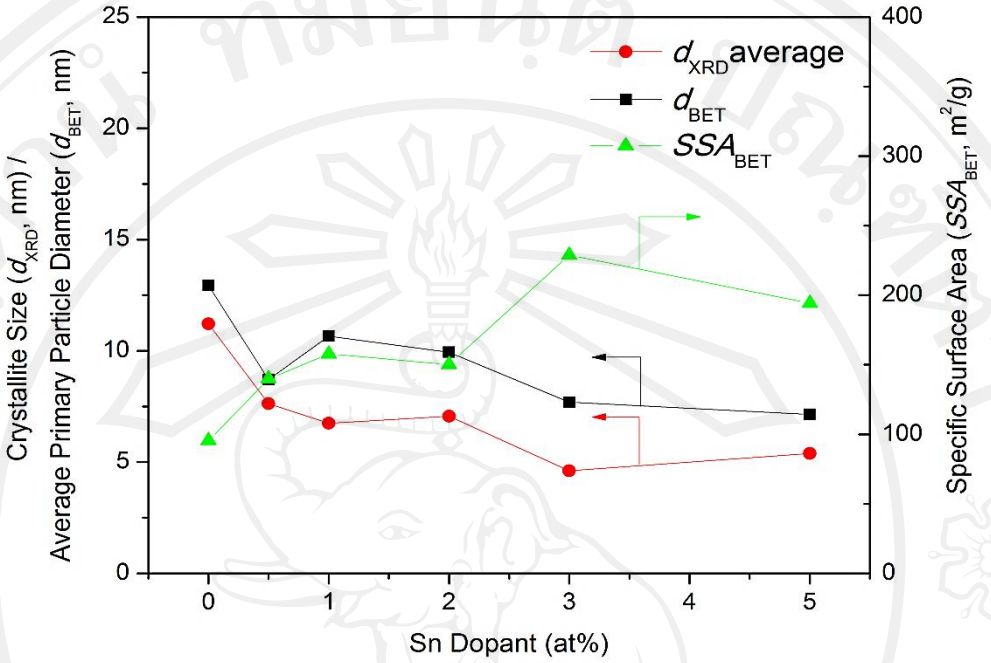

Figure 4.4 The trend of XRD-crystallite size, BET-equivalent average primary particle diameter and specific surface area of 0−5 at% Sn-doped ZnO synthesized by FSP

Figure 4.4 shows the BET results, revealing that SSA_{BET} increased from 95 to 229 m^2/g and d_{BET} reduced from approximately 11 to 5 nm as Sn concentration increased from 0 to 3 at%, followed by the slight decrease of SSA_{BET} to 194 m^2/g after doping up to 5 at%. Moreover, it can be seen that the highest SSA_{BET} of 224 m^2/g and the smallest particle size of 5 nm are obtained at Sn content of 3 at%. This indicates that the primary particle size of 3 at% Sn-doped ZnO nanostructure is very fine and highly porous. It should be noted that d_{BET} is calculated based on the assumption that particles are spherical, nonporous, smooth and monodispersed. Comparing the d_{BET} value and the d_{XRD} average value of 3 at% and 5 at% Sn-doped ZnO samples, it

ลิขสิทธิ์มหาวิทยาลัยเชียงใหม่
Copyright© by Chiang Mai University
All rights reserved

reveals that d_{XRD} and d_{BET} of 3 at% Sn-doped ZnO sample is smaller than those of 5 at% one. This may suggest that additional Sn ions more substitute into the Zn^{2+} site. It could cause defects that obstruct ZnO crystal growth, in each plane, by FSP synthesis so the d_{XRD} average and d_{BET} of 3 at% Sn-doped ZnO nanostructure are the smallest crystalline and primary particle size.

For the morphology observation, TEM images in Figure 4.5 reveal that undoped ZnO and Sn-doped ZnO nanostructures have rod-like and hexagonal/spherical morphologies. In the case of undoped ZnO (Figure 4.5(a)), the appearance of the rod-like morphologies may arise from slight oxygen deficiency, in-line with size effects caused by oxygen stoichiometry variation [139−140]. Undoped ZnO nanostructure contains the hexagonal/spherical nanostructures with diameter of 8−11 nm and rod-like nanostructure with dimensions of 9−24 nm in diameter and 22−57 nm in length. The primary rod-like ZnO nanostructure sizes of Sn-doped ZnO are clearly reduced compared to undoped ZnO. This may be correlated to the reduction of (002) crystallite sizes observed from XRD analysis. Moreover, it can be observed by comparing Figures 4.5(a) and 4.5(b) that the shape of ZnO nanostructures is altered progressively from spherical to a rod-like shape with increasing Sn concentration. This is consistent with the report by Height et al. [141] explaining that the effect of changing in the morphologies of Sn-doped ZnO synthesized by FSP is due to a large charge density of Sn^{4+} ion, significantly deforming the ZnO lattices. From high resolution TEM image of Sn-doped ZnO nanostructures in Figure 4.5(c), the spacing between the lattice planes of the crystallite nanorod was measured to be ~0.28 nm in axial direction, consistent with (100) plane which is perpendicular to

ลิขสิทธิ์มหาวิทยาลัยเชียงใหม่
Copyright© by Chiang Mai University
All rights reserved

(002) plane. This indicates that the ZnO nanorods grow along the c-axis or $\langle 2110 \rangle$ direction.

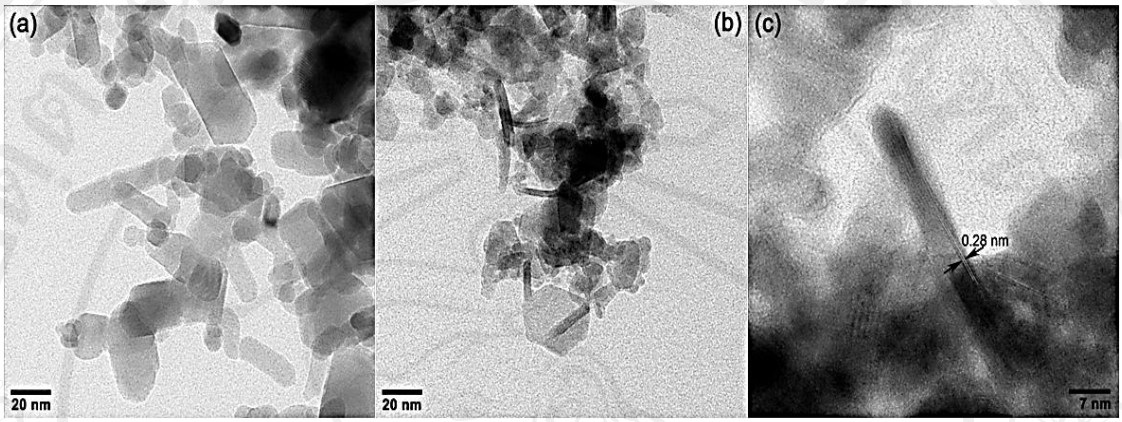

Figure 4.5 TEM images of (a) undoped ZnO, and (b) and (c) 5 at% Sn-doped ZnO nanostructures

Figure 4.6 illustrates the surface microstructure of SEM images and EDS analysis of undoped ZnO, 2 and 5 at% Sn-doped ZnO nanostructures. The results confirm that the agglomerated nanostructure size decreased and the elemental composition of Sn element in ZnO nanostructure increased as the intended Sn doping concentration increased. The atomic composition ratio of Zn:Sn is shown in EDS spectra of Figure 4.6. It can be seen that the actual doping concentration is rather close to the calculated doping concentration. Thus, FSP technique could offer well controlled doping as well as uniform dopant dispersion.

ลิขสิทธิ์มหาวิทยาลัยเชียงใหม่
Copyright© by Chiang Mai University
All rights reserved

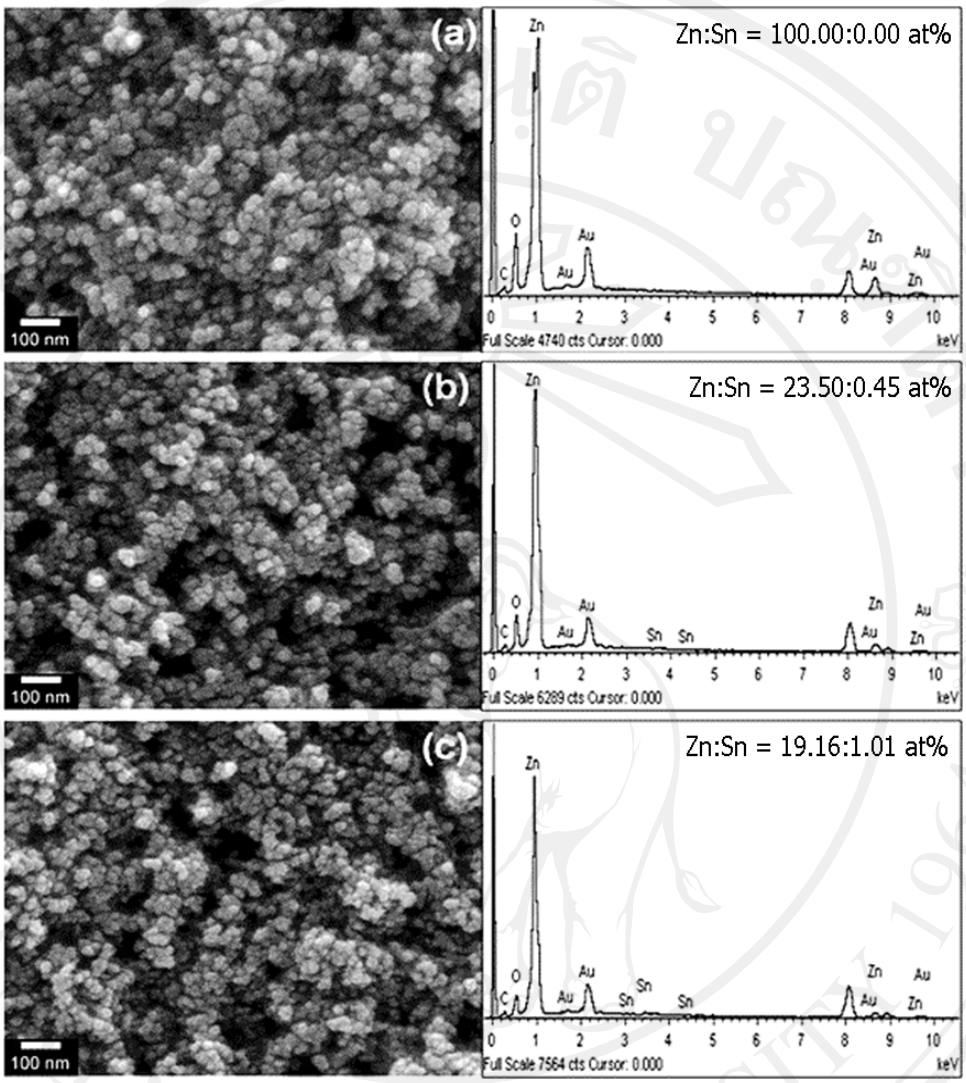

Figure 4.6 SEM images of (a) undoped ZnO, (b) 2 at% Sn-doped ZnO and (c) 5 at% Sn-doped ZnO nanostructures with EDS analysis of all covered area of the SEM image, inserted at the side of the images

4.2 Gas sensing application

According general metal oxide semiconductor behaviors, the deviation of stoichiometry, point defects, such as O vacancies are normally formed on ZnO surfaces at high temperatures. These factors are very significant to gas sensing since the electrons originate from intrinsic oxygen vacancies and are trapped at the surface,

ลิขสิทธิ์มหาวิทยาลัยเชียงใหม่
Copyright© by Chiang Mai University
All rights reserved

resulting in electron-depleted surface region. This depleted region of majority carrier extends a few Debye lengths into the bulk. The conductivity variations occurred at the surface of ZnO grains as a result of gas-ionosorption cause the change in band bending or space-charge layer. In the case of nanoparticles, the depleted zones start to overlap and the adjacent Schottky barriers fall below the thermal energy, leading to flat-band expected enhanced gas sensitivity [126, 142].

The maximum sensitivity depending on sensing layers are all reachable to oxygen and analyte molecules in ambient so a lower film thickness including its porosity contributes to higher sensitivity and shorter response time [143−144]. The thickness of sensor film, which significantly affects gas sensitivity, was analyzed by cross-section FESEM as shown in Figure 4.7. The thickness of 2 at% Sn-doped ZnO sensing films is approximately 2.2 μm (Figure 4.7(a)). The EDS line scan spectra confirmed the compositions of the film from the corresponding signal of the elements. Moreover, the upper surface film in Figure 4.7(a) after gas-sensing test as shown in Figure 4.7(d) indicates larger sub-nanometer grain size than that before gas-sensing test in Figure 4.7(c) (Figures 4.7(c) and 4.7(d) images are of the same magnification at 100K).

The gas sensing properties were characterized in terms of a changing in resistance, response and response time. As an n-type semiconductor, the percent reduction of sensor resistance is also an alternative measure of gas-sensing response, namely $S = R_a / R_g$ defining R_g as the resistance level when the gas is present and R_a as the level in air. Response time is calculated from the time taken to test reach 90% of $(R_a - R_g)$ after the gas injection. For p-type semiconductor gas sensor, the definitions are reversed. The gas-sensing response is calculated from the dynamic

ลิขสิทธิ์มหาวิทยาลัยเชียงใหม่
Copyright© by Chiang Mai University
All rights reserved

variation of conductance due to gas pulses introduction and plotted versus various parameters including operating temperature and gas concentration.

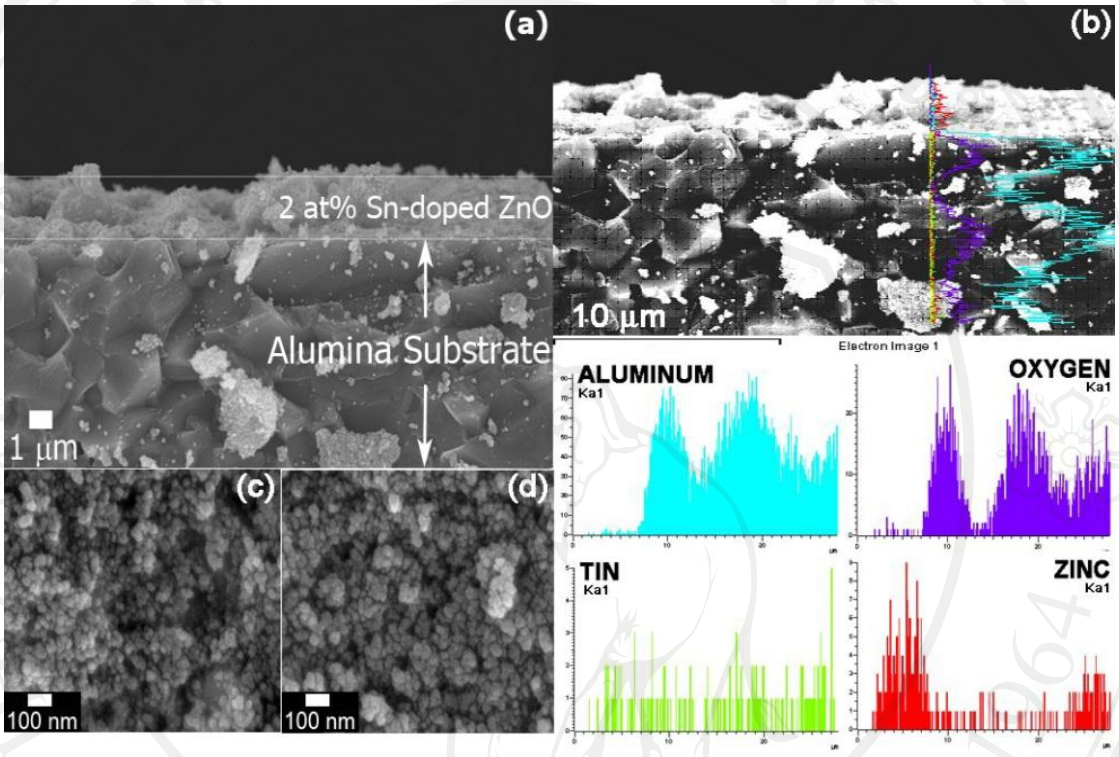

Figure 4.7 FESEM-EDS analysis of 2 at% Sn-doped ZnO sensing film: (a) cross-section FESEM image, (b) EDS line scan mode indicated as the corresponding signal of the elements composition, (c) top view before gas sensing test and (d) top view after gas sensing test

4.2.1 The effect of operating temperatures on gas response of undoped ZnO and Sn-doped ZnO sensors

Figures 4.8(a), (b), (c) and (d) show the gas response of undoped ZnO, and 2, 3 and 5 at% Sn-doped ZnO sensors, respectively, to acetone ($(CH_3)_2CO$; 400 ppm), ethanol (C_2H_5OH; 1,000 ppm), hydrogen (H_2; 50,000 ppm) and methane (CH_4; 50,000 ppm) at different operating temperatures ranging from 200 to 400°C. It was

ลิขสิทธิ์มหาวิทยาลัยเชียงใหม่
Copyright© by Chiang Mai University
All rights reserved

found that the same trend response of both undoped ZnO and Sn-doped ZnO sensors to C_2H_5OH and H_2 gases continuously increased when the operating temperatures increased up to 400°C while their responses to $(CH_3)_2CO$ and CH_4 gas showed optimal operating temperature at 350°C. These results were consistent with other researches [145−148] observing C_2H_5OH and H_2 response of ZnO sensors and indicating that the highest response was at optimal operating temperature of 400°C in air. In event that tested gas sensing in different atmosphere, gas sensor exhibited dissimilar optimal operating temperatures due to the effect of the atmosphere on the intrinsic defect concentration [149]. Moreover, Bhattacharyya et al. [150] indicated that the highest 1% CH_4 response of ZnO was at optimal operating temperature of 350°C in air for Au contact. In case of $(CH_3)_2CO$ sensing using ZnO nanoparticles, Zhu et al. [151] reported that the $(CH_3)_2CO$ sensing was improved when the operating temperature increase up to around 350°C and then it was deteriorated when the operating temperature around 400°C. However, in order to reach the highest gas species sensing, the optimal operating temperature should be operated in a temperature range where reversible chemisorption takes place or provided alternative ways to induce desorption [126]. In chemical processes, the adsorption/desorption having activation energies, depend on the shape and the size of the nanocrystals for the reason that they influence on the concentration of the adsorbed species and on the type of bonding to the surface that took place [152]. Therefore, the reaction between C_2H_5OH and H_2, and adsorbed oxygen was improved due to the increasing operating temperature, causing the measured response increased. On the other hand, $(CH_3)_2CO$ and CH_4 desorption phenomena became predominant with the increasing operating temperature up to 400°C causing the measured response to decrease. As lower

ลิขสิทธิ์มหาวิทยาลัยเชียงใหม่
Copyright© by Chiang Mai University
All rights reserved

operating temperatures, the response was rather low because the absorbed gases are not sufficiently activated to react with surface oxygen species. At optimal operating temperature, the fastest response time of <3 s were found towards 1,000 ppm C_2H_5OH response of Sn-doped ZnO sensors and 50,000 ppm CH_4 response of 3−5 at% Sn-doped ZnO sensors. The response time is also a function of gas concentration, additive concentration and operating temperature [153−155]. However, the response rate of ZnO doped with Sn towards H_2 gas was still rather low than other target gas species at the same operating temperature. Figure 4.8 showed that the tendency of the gas response of the sensors as a function of operating temperature was contrary with the tendency of the response time.

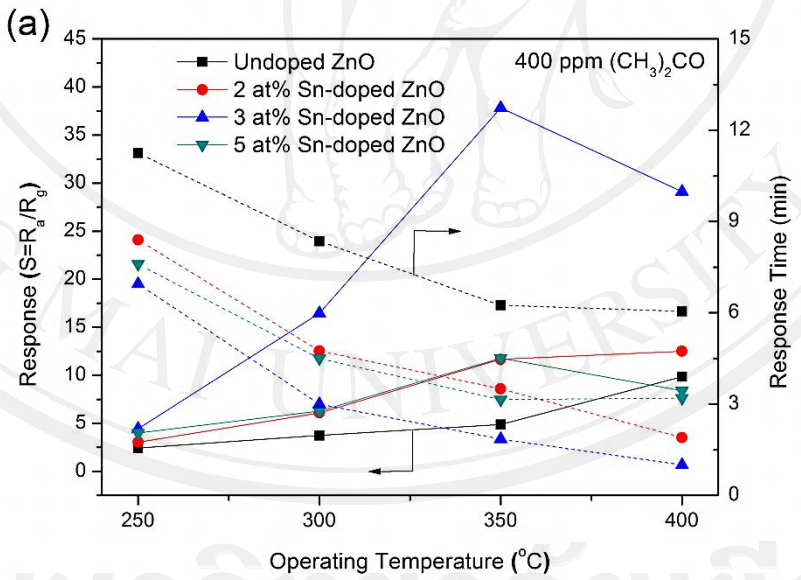

Figure 4.8 Relationship between (a) 400 ppm $(CH_3)_2CO$ response/response time, and operating temperatures

ลิขสิทธิ์มหาวิทยาลัยเชียงใหม่
Copyright© by Chiang Mai University
All rights reserved

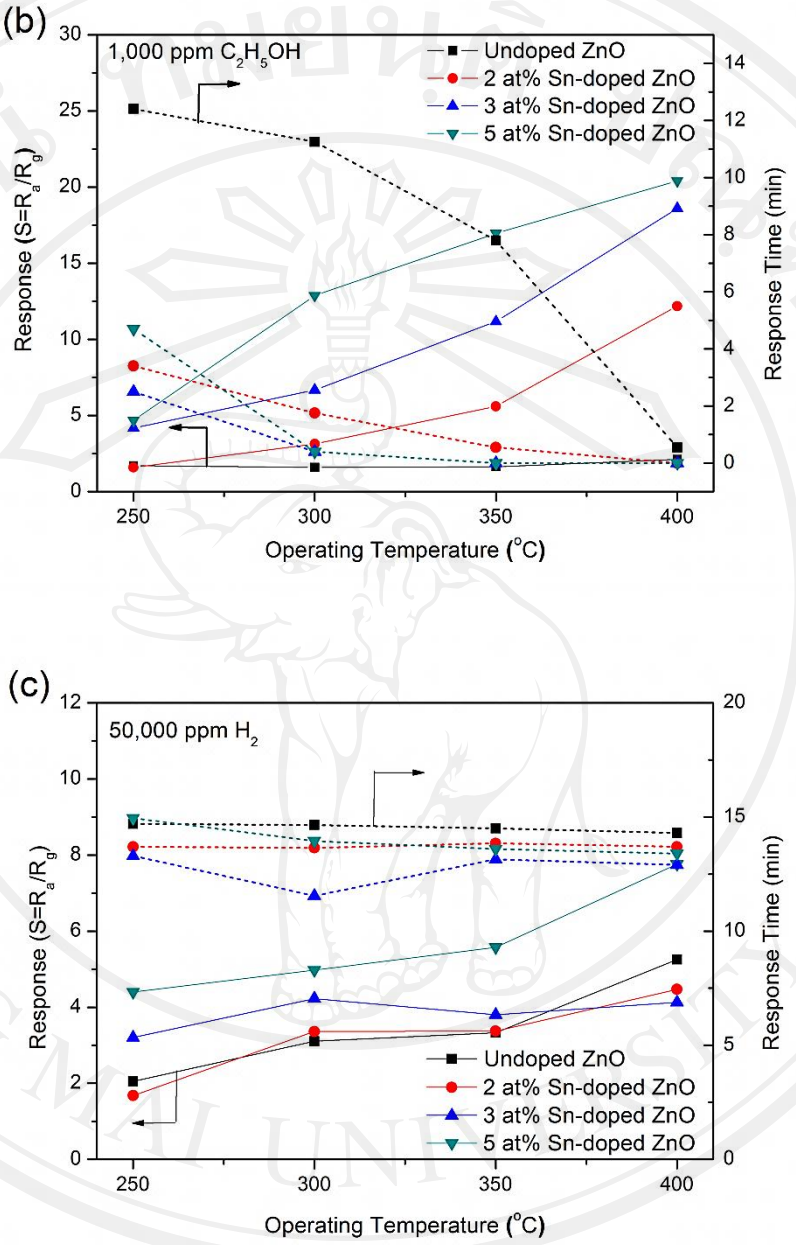

Figure 4.8 (cont.) Relationship between (b) 1,000 ppm C_2H_5OH, and (c) 50,000 ppm H_2 response/response time, and operating temperatures

ลิขสิทธิ์มหาวิทยาลัยเชียงใหม่
Copyright© by Chiang Mai University
All rights reserved

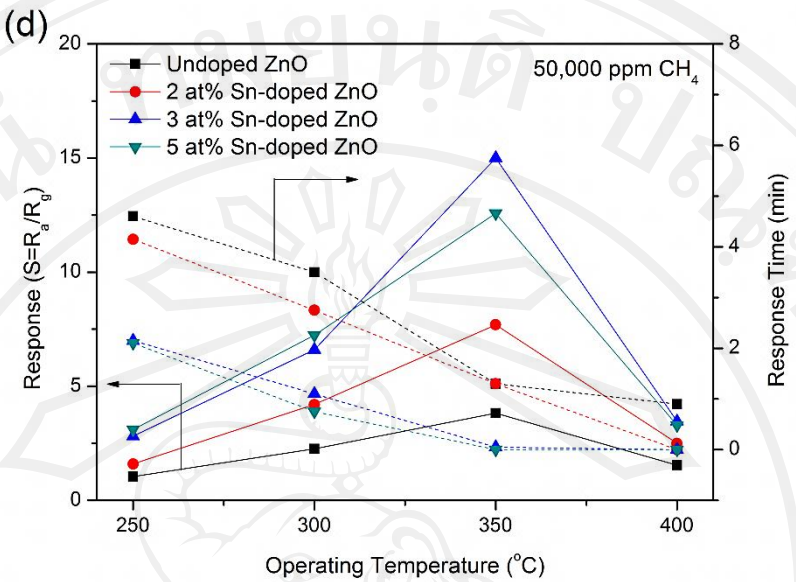

Figure 4.8 (cont.) Relationship between (d) 50,000 ppm CH_4 response/response time, and operating temperatures

4.2.2 The effect of gas species on change in conductivity of undoped ZnO and Sn-doped ZnO sensors

Figures 4.9 (a), (b), (c) and (d) show the change in conductivity of the sensors under exposure to $(CH_3)_2CO$ (100−400 ppm), C_2H_5OH (300−1,000 ppm), H_2 (5,000−20,000 ppm), CH_4 (10,000−50,000 ppm) gases, respectively, at operating temperature of 400°C. The gas sensing results towards H_2 and CH_4 obtained in terms of high concentrations since the sensor response was not very good. The relationship of response on concentration was confirmed that it depended on the law for metal-oxide semiconductor sensors, $S = a[C]^b$ [156] where C represents gas concentration, and a and b are constants. In Figures 4.9(c) and (d), as the steady equilibrium of H_2 and CH_4 curves did not show the saturated effect, it may be because of limited absorption reversion or desorption of the gases. The current of undoped ZnO and Sn-

ลิขสิทธิ์มหาวิทยาลัยเชียงใหม่
Copyright© by Chiang Mai University
All rights reserved

doped ZnO sensors increased upon the exposure to $(CH_3)_2CO$, C_2H_5OH and CH_4 gases (reducing gas), confirming that they are n-type semiconductor. For gas sensing mechanism, oxygen adsorbed on the surface of ZnO sensors, extracting an electron from the conduction band to ionize into O^-, O^{2-} or O_2^- (O^- was expected that it was stabilized on surface particularly at operating temperature of more than 320°C and this ion has often appeared on mechanism for catalytic reaction over ZnO) [157].

The reaction mechanism between $(CH_3)_2CO$ (4.2−4.3), C_2H_5OH (4.4−4.6), H_2 (4.7) and CH_4 (4.8) and ionic oxygen (O^-) can be explained by Equations (4.2)−(4.8) [158−161] as follows:

$$CH_3COCH_3(gas) + O^- \Rightarrow CH_3CO^+CH_2 + OH^- + e^- \quad (4.2)$$

$$CH_3COCH_3(gas) + OH^- \Rightarrow CH_3CHO + CH_3O^- \quad (4.2.1)$$

$$CH_3CHO + O(bulk) \Rightarrow CH_3COOH + O(vacancies) \quad (4.2.2)$$

$$CH_3COCH_3(gas) + O^- \Rightarrow CH_3^+CO + CH_3O^- + e^- \quad (4.3)$$

$$CH_3^+CO \Rightarrow CH_3^+ + CO \quad (4.3.1)$$

$$CO + O^- \Rightarrow CO_2 + e^- \quad (4.3.2)$$

$$CH_3CH_2OH(gas) + 6O^- \Rightarrow 2CO_2 + 3H_2O + 6e^- \quad (4.4)$$

$$CH_3CH_2OH(gas) + O^- \Rightarrow CH_3CHO + H_2O + e^- \quad (4.5)$$

$$CH_3CH_2OH(gas) + O^- \Rightarrow C_2H_5O^- + H_2O \quad (4.6)$$

$$C_2H_5O^- \Rightarrow C_2H_5O + e^- \quad (4.6.1)$$

$$H_2 + O^- \Rightarrow H_2O + e^- \quad (4.7)$$

$$CH_4 + 4O^- \Leftrightarrow CO_2 + 2H_2O + e^- \quad (4.8)$$

ลิขสิทธิ์มหาวิทยาลัยเชียงใหม่
Copyright© by Chiang Mai University
All rights reserved

Nevertheless, change in the current to H_2 gas of ZnO sensors decreased indicating that they could tunable to p-type semiconductor when exposed to high concentration of H_2 and operated at high temperature. From band diagram of semiconductor, the total amount of surface charge varies with the location of Fermi level, whereas the substrate changes from n-type to p-type due to the fact that the net charge of the absorbate changes from negative to positive following Park and Akbar [123]. Thus, the Fermi level of the n-type ZnO films may have been changed adjacent to the top of valence band when reacted with H_2 gas at high concentration and operating temperature. Likewise, Liu et al. [162] and Kobrinsky et al. [163] investigated H_2 sensing properties of ZnO films at high concentration and operating temperature and found that the conductivity types of ZnO films converted from p-type to n-type.

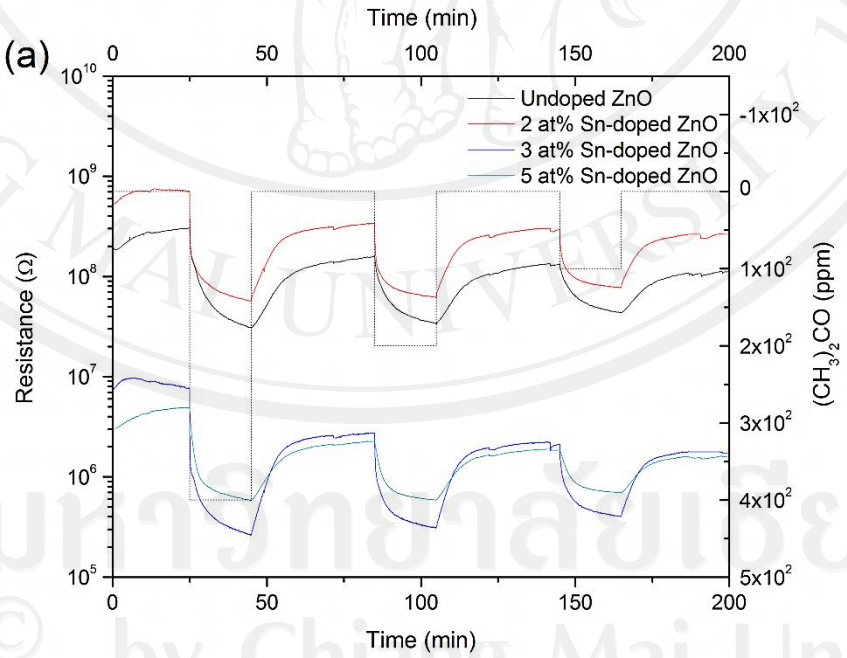

Figure 4.9 Change in the conductivity of undoped ZnO, and 2, 3 and 5 at% Sn-doped ZnO sensors under exposure to (a) $(CH_3)_2CO$ at 400°C during backward cycle

ลิขสิทธิ์มหาวิทยาลัยเชียงใหม่
Copyright© by Chiang Mai University
All rights reserved

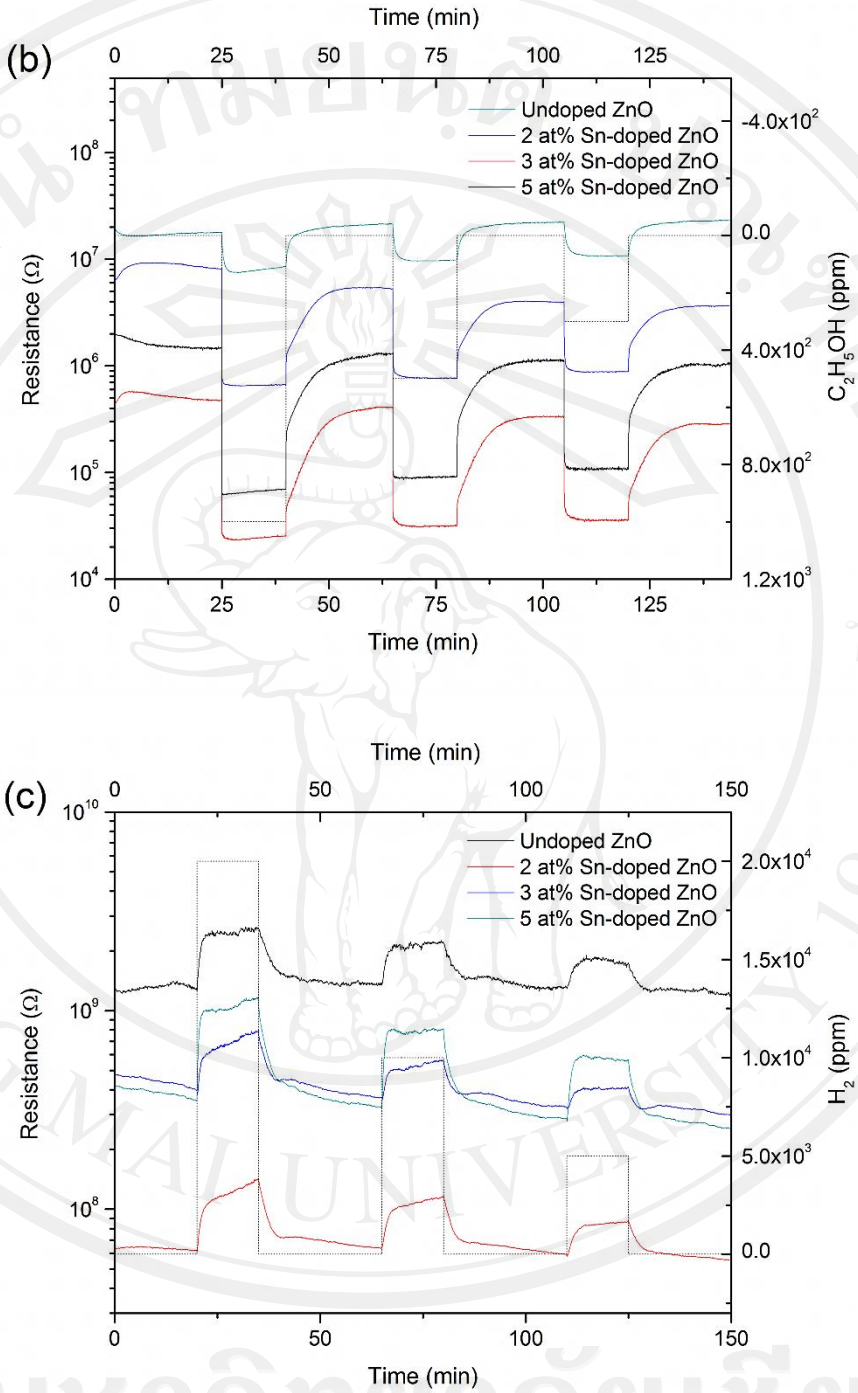

Figure 4.9 (cont.) Change in the conductivity of undoped ZnO, and 2, 3 and 5 at% Sn-doped ZnO sensors under exposure to (b) C_2H_5OH, and (c) H_2 at 400°C during backward cycle

ลิขสิทธิ์มหาวิทยาลัยเชียงใหม่
Copyright© by Chiang Mai University
All rights reserved

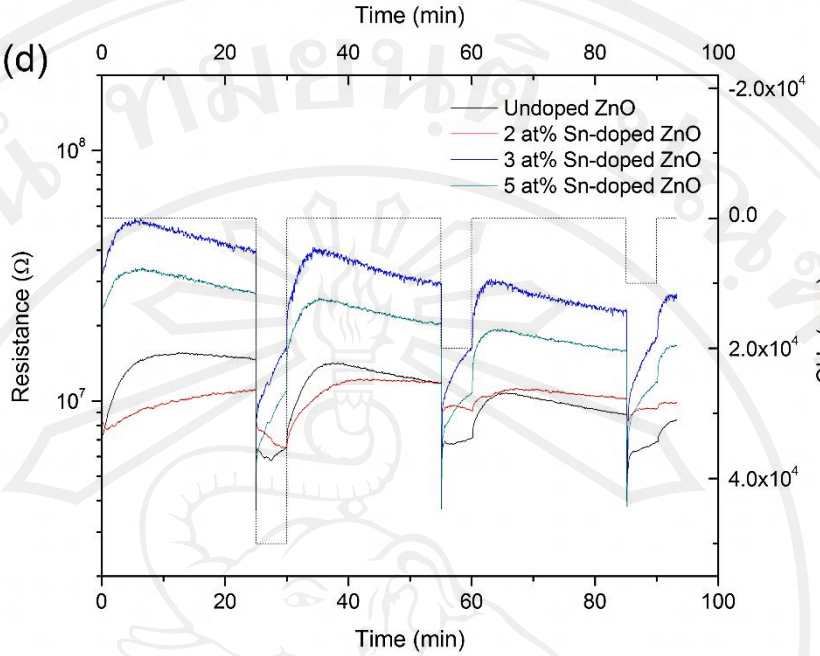

Figure 4.9 (cont.) Change in the conductivity of undoped ZnO, and 2, 3 and 5 at% Sn-doped ZnO sensors under exposure to (d) CH_4 at 400°C during backward cycle

Figure 4.10 shows the sensing performance of the 5 and 3 at% Sn-doped ZnO sensors investigated as a function of C_2H_5OH and H_2, and $(CH_3)_2CO$ and CH_4 gas concentrations, respectively, at operating temperature of 400°C. Under the consideration of the lowest limitation response value, a value of 1.1, calculated detection limits for $(CH_3)_2CO$, C_2H_5OH, H_2 and CH_4 were approximately 47.0, 4.9, 1,085.6 and 3,079.1 ppm, respectively. The comparative data were clearly seen that ZnO doped with Sn (5 at%) sensors exhibiting the best response towards C_2H_5OH with the low detection limit.

ลิขสิทธิ์มหาวิทยาลัยเชียงใหม่
Copyright© by Chiang Mai University
All rights reserved

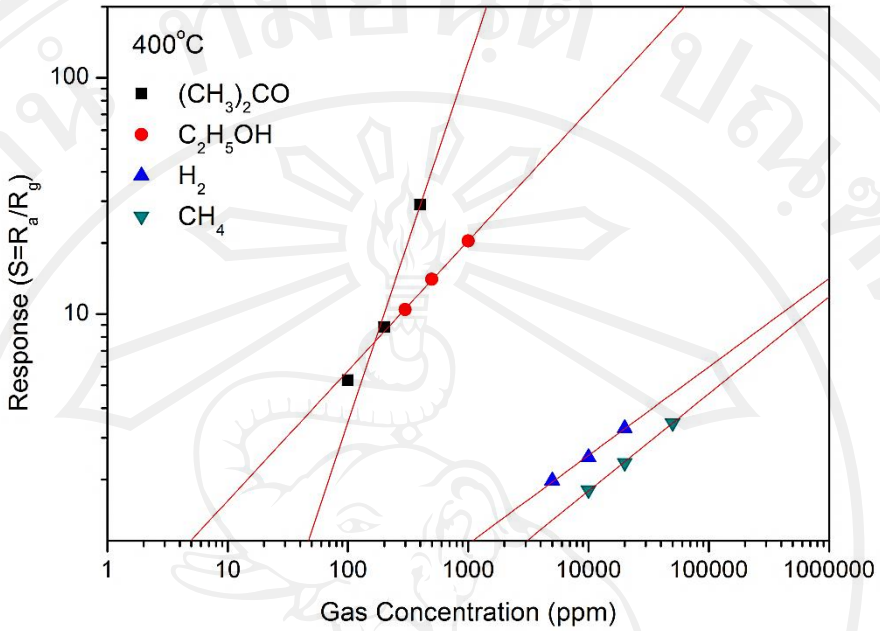

Figure 4.10 The gas sensing response of 5 at% Sn-doped ZnO to C_2H_5OH and H_2, and 3 at% Sn-doped ZnO to $(CH_3)_2CO$ and CH_4, as a function of concentration at operating temperature of 400°C

4.2.3 The gas response comparison of undoped ZnO and Sn-doped ZnO sensors

Figure 4.11 shows the response comparison of the type of sensors (undoped ZnO and 2−5 at% Sn-doped ZnO) to 100 ppm $(CH_3)_2CO$ and C_2H_5OH vapors, and 10,000 ppm H_2 and CH_4 gases at the operating temperature of 400°C. At 3 at% Sn-doped ZnO, it gave the similar response value of 100 ppm $(CH_3)_2CO$ and C_2H_5OH. On the contrary, at 5 at% Sn-doped ZnO, it gave the response value of C_2H_5OH more clearly than $(CH_3)_2CO$ as approximately 2.2 times. In particular, it revealed that the excellent C_2H_5OH response was better than undoped ZnO as approximately 3.5 times. When the response of 10,000 ppm H_2 and CH_4 was compared, it was found that 3 at%

ลิขสิทธิ์มหาวิทยาลัยเชียงใหม่
Copyright© by Chiang Mai University
All rights reserved

Sn-doped ZnO sensor gave the highest response of 1.80 to CH_4 gas and 5 at% Sn-doped ZnO sensor gave the highest response of 2.48 to H_2 gas. ZnO nanostructure electrical properties have been characterized in the presence of different gases, the results highlight remarkable response to $(CH_3)_2CO$ and C_2H_5OH. These results correspond with the ZnO gas sensor researches towards different gases reported by Comini et al. [156], Zeng et al. [164], Qi et al. [165], Kim et al. [166] and Hwang et al. [167]. However, the difference in the response factor for $(CH_3)_2CO$, C_2H_5OH, H_2 and CH_4 gases may be related to diffusion coefficient being different into the pore structure of sensor materials according to the composition of basic material and doping level [168−170].

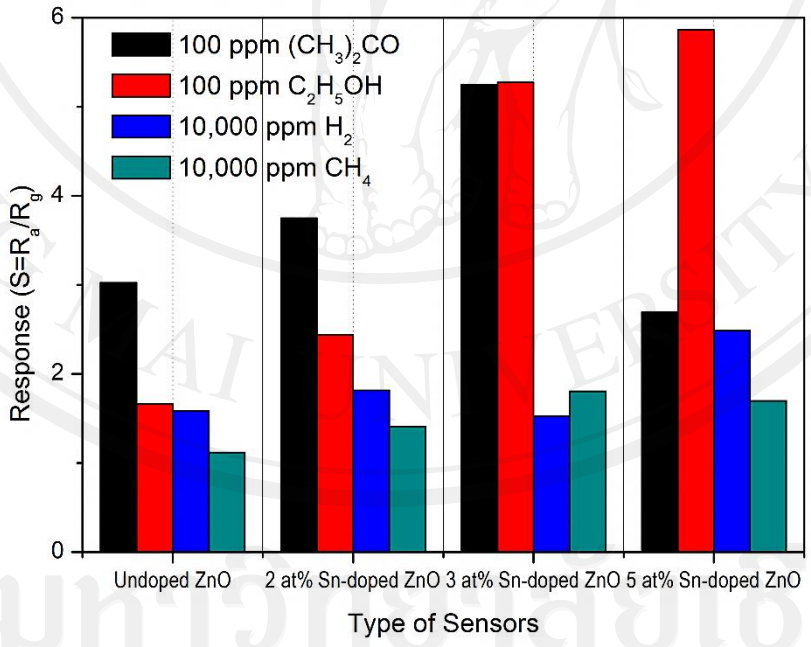

Figure 4.11 The gas response of undoped ZnO, and 2, 3 and 5 at% Sn-doped ZnO sensors at 100 ppm of $(CH_3)_2CO$ and C_2H_5OH, and at 10,000 ppm of H_2 and CH_4 under the operating temperature of 400°C

ลิขสิทธิ์มหาวิทยาลัยเชียงใหม่
Copyright© by Chiang Mai University
All rights reserved

For Sn-doped ZnO material, it is well known that Sn acts as a source of donor, which introduces deep states in the bandgap and results in the gap narrowing [171−172]. Therefore, it can be inferred that Sn-doped ZnO sensor has the reduced space-charge layer thickness compared to undoped ZnO sensor because Sn is a good candidate as an n-type dopant in ZnO when it substitutes Zn^{2+} site resulting in two more free electrons to contribute to the electronic conduction. This is consistent with Shishiyanu et al. [84], who revealed by rapid photothermal processing (RPP) technique that the electrical resistivity of Sn-doped ZnO film decreased with increasing temperature because the loss of adsorbed oxygen increased the donor concentration of the surface and thereby enhanced the conductance. Thus, it will also be good for detection of oxidizing gases like NO_2.

From our results, the gas-sensing response is considerably improved due to Sn doping in ZnO nanostructure film sensors. Likewise, Trinh et al. [85] reported that Sn-doped ZnO nanoparticle thin film exhibited better C_2H_5OH-sensing response than undoped ZnO nanoparticle thin film. Their special physical characteristic as revealed by XRD, TEM and BET analyses is attributed to the improved gas-sensing response of Sn-doped ZnO sensors. Sn-doped ZnO nanostructures synthesized by FSP clearly possess smaller grain sizes as Sn content increases. When the grain size is smaller than twice of the space-charge layer thickness ($D_a < 2L_D$, where D_a is the grain size diameter and L_D is the space-charge layer thickness with L_D value of ZnO = 7.5 nm [85]), the resistance of the sensing films are mainly determined by fully depleted grains [142].

ลิขสิทธิ์มหาวิทยาลัยเชียงใหม่
Copyright© by Chiang Mai University
All rights reserved

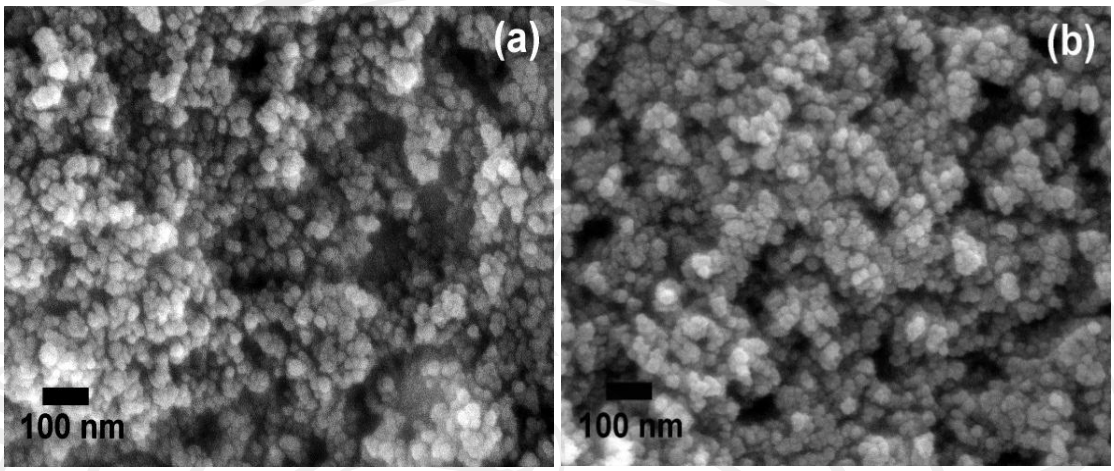

Figure 4.12 SEM image comparisons in the same scale of (a) original FSP-made 2 at% Sn-doped ZnO nanostructures, and (b) prepared 2 at% Sn-doped ZnO film

Thus, the sensitivity of the sensor is improved with decreasing grain size as long as the depletion region extends over the entire grain. Since the ZnO nanostructure films prepared for gas sensors went through the temperature annealing process at 400°C, their grain sizes may change considerably from that of their raw FSP-made nanostructures. To verify the possible change, the morphologies of 2 at% Sn-doped ZnO nanostructure film and its raw FSP-made nanostructures were examined by SEM as illustrated in Figures 4.12(a) and 4.12(b), respectively. It is clear that the average agglomerate size of the ZnO nanostructures in prepared film (Figure 4.12(a)) is almost identical to that of the original FSP-made ZnO nanostructures (Figure 4.12(b)), so grain size of the prepared film is not significantly different from that of its raw material. Therefore, it can be noticed that 3−5 at% Sn-doped ZnO sensor exhibited the best gas-sensing performance due to its very small grain size. Moreover, the amount of free electrons in ZnO structure from doping Sn metal will help greatly in the change of the sensor resistance. The optimum Sn content for gas

ลิขสิทธิ์มหาวิทยาลัยเชียงใหม่
Copyright© by Chiang Mai University
All rights reserved

sensing in the range of 3−5 at% is similar to other reported Sn-doped ZnO sensors for detecting C_2H_5OH and NO_2, whose optimum Sn concentrations are around 4 or 5 at% [84−85]. The difference in optimum dopant concentration obtained from various preparation methods may be due to the variation of actual doping amount, dopant distribution and physiochemical properties of differently prepared ZnO sensor.

4.3 Photocatalyst application

4.3.1 UV-vis absorption characteristics

The optical studies are essential for photocatalytic properties of the samples. The UV-vis absorption spectra of the FSP-synthesized ZnO nanostructures are shown in Figure 4.13. The photon energy of ZnO nanostructures was converted by using $E_g = hc/\lambda$ equation, where h is plank's constant, c is velocity of light, and λ is wavelength. The ZnO samples exposed a characteristic absorption peak of the UV-vis absorption spectra. The crystalline quality of a semiconductor has been related to the appearance of excitonic absorption in its optical absorption spectrum [173]. It is clear from the spectra that there is a shift in the the excitonic absorption peaks of higher Sn doping in ZnO nanostructures towards higher photon energy region.

The absorption spectra via technique of the samples obtained from two components: dispersed light due to scattering counted as absorbed light by the spectrophotometer, and optical absorption due to electronic transitions in the samples. The peaks in the absorption spectra do not correspond to the true optical bandgap of ZnO, which is about 3.3 eV (at room temperature). ZnO bandgap (E_g) can be obtained

ลิขสิทธิ์มหาวิทยาลัยเชียงใหม่
Copyright© by Chiang Mai University
All rights reserved

from absorption spectra through the first derivative of absorbance with respect to photon energy. The E_g is associated to the maximum in the spectrum [174].

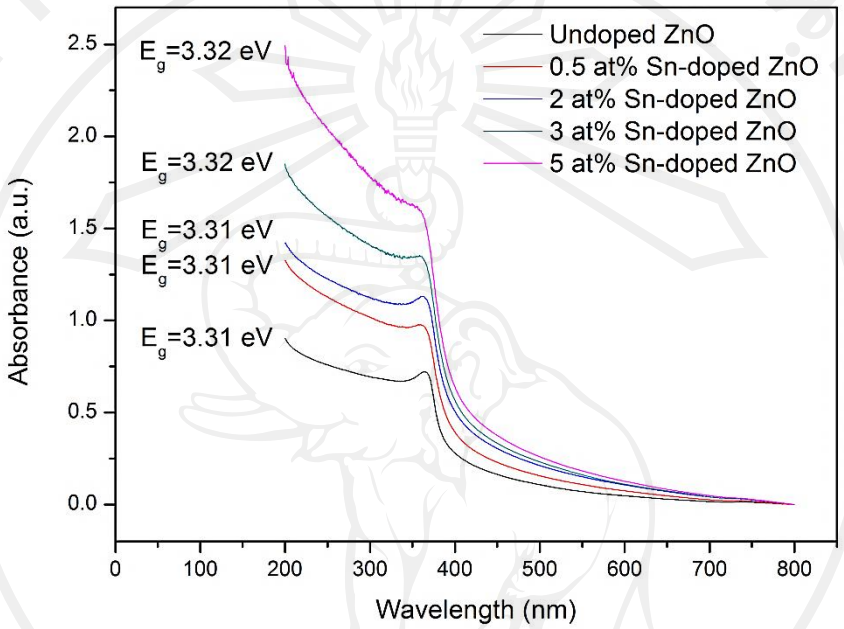

Figure 4.13 UV-Vis absorption spectra of ZnO nanostructures with 0−5 at% Sn doping concentration

Figure 4.14 shows the derivative spectra of the samples and the bandgap of the nanostructures calculated were found to be 3.31 eV for 0, 0.5 and 2 at% Sn doped ZnO, and 3.32 eV for 3 and 5 at% Sn doped ZnO which clearly exhibiting a blue-shift for higher Sn doping. The energy bandgap of a semiconductor depends on the crystal size, according to quantum confinement theory. Since the dimension of nanomaterials is much larger than the excitonic Bohr radius of 1.8 nm for ZnO [175], they will experience a weak confinement circumstance. An expression based on the effective mass model for the energy gap is

ลิขสิทธิ์มหาวิทยาลัยเชียงใหม่
Copyright© by Chiang Mai University
All rights reserved

$$E_g = E_g^{bulk} + \frac{h^2}{2\mu r^2} \tag{4.9}$$

where E_g^{bulk} is the bulk ZnO bandgap (3.37 eV), r is the radius of the nanoparticles, $1/\mu = 1/m_e + 1/m_h$ (m_e and m_h being the electron and hole effective masses, respectively) and h is Planck's constant [173].

This tendency of optical bandgaps of ZnO doped with Sn in higher concentration was consistent with the literatures [77, 176−178]. This is the reasons for Sn^{4+} (0.74 Å) ions to substitute Zn^{2+} (0.83 Å) ions into the ZnO lattice, given the similarity in their ionic radii. The same reason on the physical characteristics of these nanostructures was reported by Wetchakun et al. [179]. This phenomenon was explained by semiconductor-metal transition theory indicating that bandgap increases when the impurity is kept under the Mott critical density in heavily doped semiconductor [177]. However, the results contradicted with Wu et al. [180] that the slightly decrease of bandgap, being result from doping induced band edge bending. In this case, because of Schottky contact effect, Sn particle clusters may deposited outside on the ZnO surface. This assumption hardly affects the optical absorption characteristics of ZnO than Sn incorporation into the crystal lattice of ZnO, given by the authors [180]. Moreover, their XRD results on the ZnO crystallite size remained unchanged.

ลิขสิทธิ์มหาวิทยาลัยเชียงใหม่
Copyright© by Chiang Mai University
All rights reserved

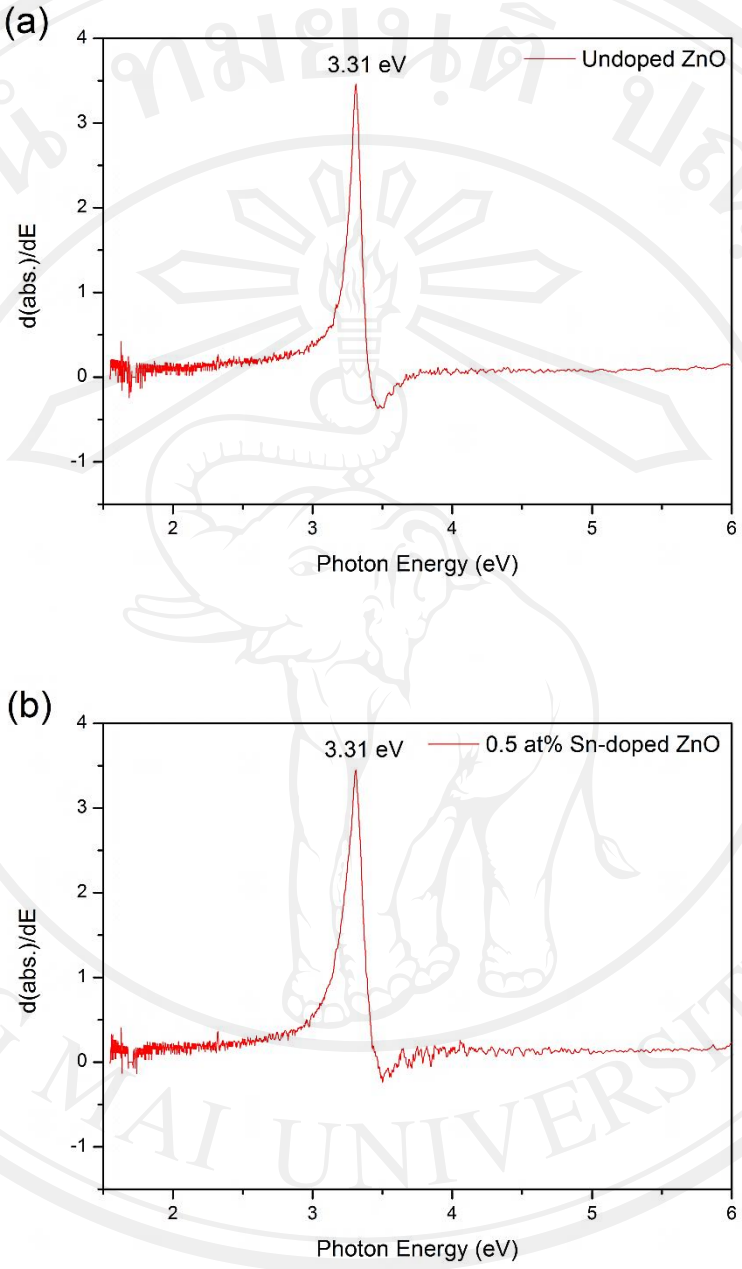

Figure 4.14 First derivative of absorbance (abs.) with respect to photon energy (E) of (a) undoped ZnO and (b) 0.5 at% Sn-doped ZnO

ลิขสิทธิ์มหาวิทยาลัยเชียงใหม่
Copyright© by Chiang Mai University
All rights reserved

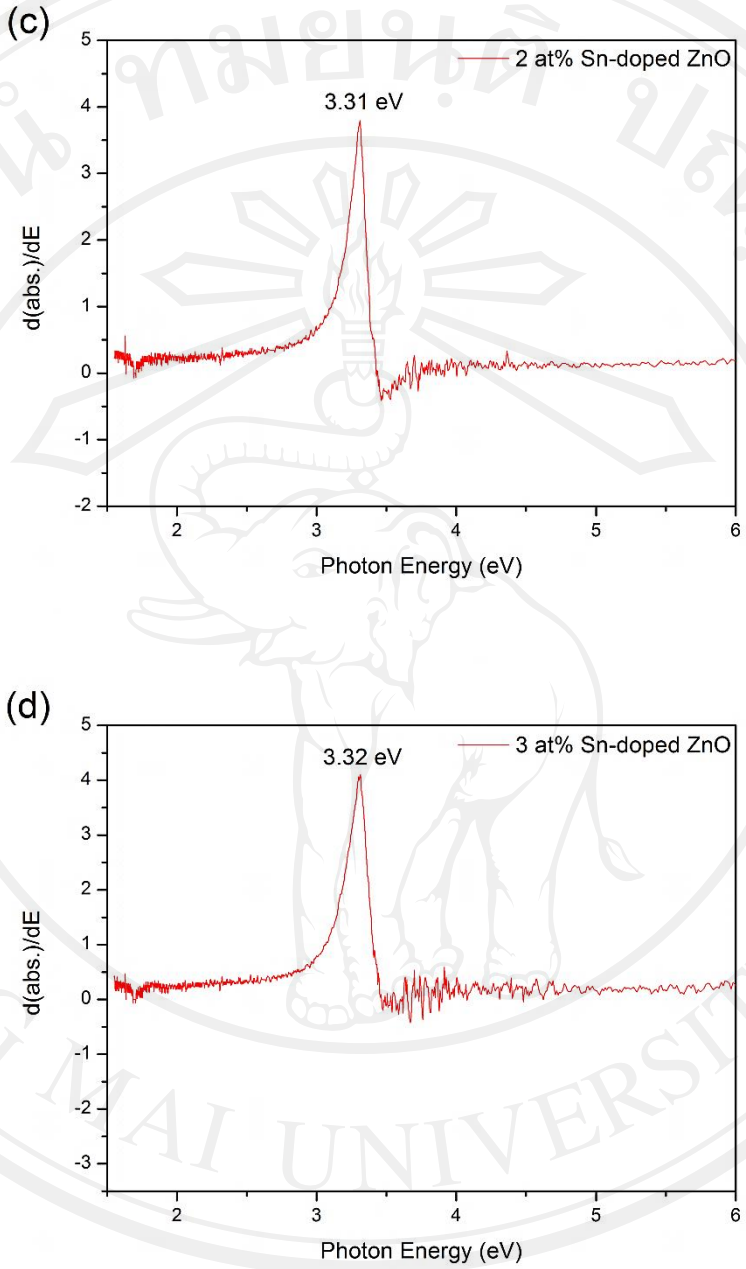

Figure 4.14 (cont.) First derivative of absorbance (abs.) with respect to photon energy (E) of (c) 2 at%, and (d) 3 at% Sn-doped ZnO

ลิขสิทธิ์มหาวิทยาลัยเชียงใหม่
Copyright© by Chiang Mai University
All rights reserved

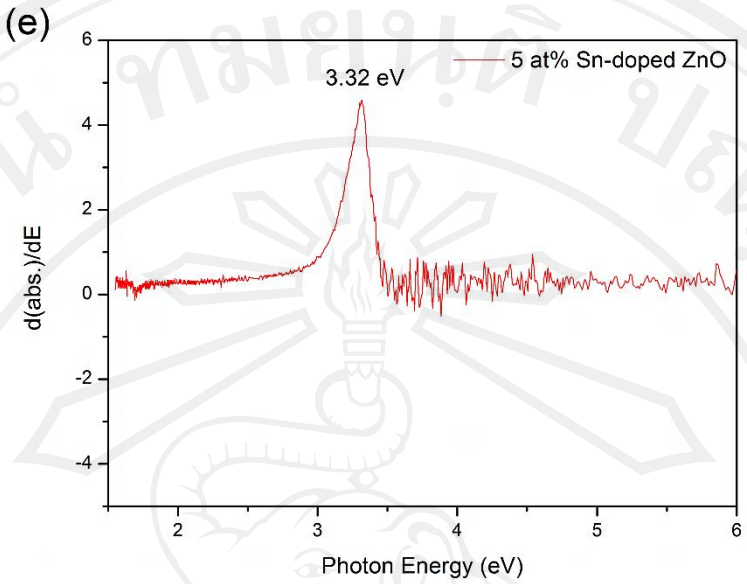

Figure 4.14 (cont.) First derivative of absorbance (abs.) with respect to photon energy (E) of (e) 5 at% Sn-doped ZnO

4.3.2 Phenol and methanol photodegradation properties

Irradiation time change as a function of phenol (C_6H_5OH) concentrations (C_t) is illustrated in Figure 4.15. In Figure 4.15(a), the rate of C_6H_5OH photodegradation in the presence of ZnO-based photocatalyst was faster than that without the catalyst. This was previously explained to be due to the formation of $OH^{\bullet}$ radicals as well as the direct oxidation by photogenerated holes, etc. [181]. This is similar with oxidation pathways to those of TiO_2. Following many previous researches on C_6H_5OH degradation process, catechol, hydroquinone (HQ), benzoquinone (BQ) and trihydoxybenzene, (THB) were identified as intermediate compounds [94]. However, doping ZnO with Sn did not enhance the C_6H_5OH photodegradation. By using undoped ZnO as a catalyst, C_6H_5OH was completely removed within 50 min.

ลิขสิทธิ์มหาวิทยาลัยเชียงใหม่
Copyright© by Chiang Mai University
All rights reserved

However, the complete C_6H_5OH degradation took longer time up to 100 min in the case of 5 at% Sn-doped nanostructures.

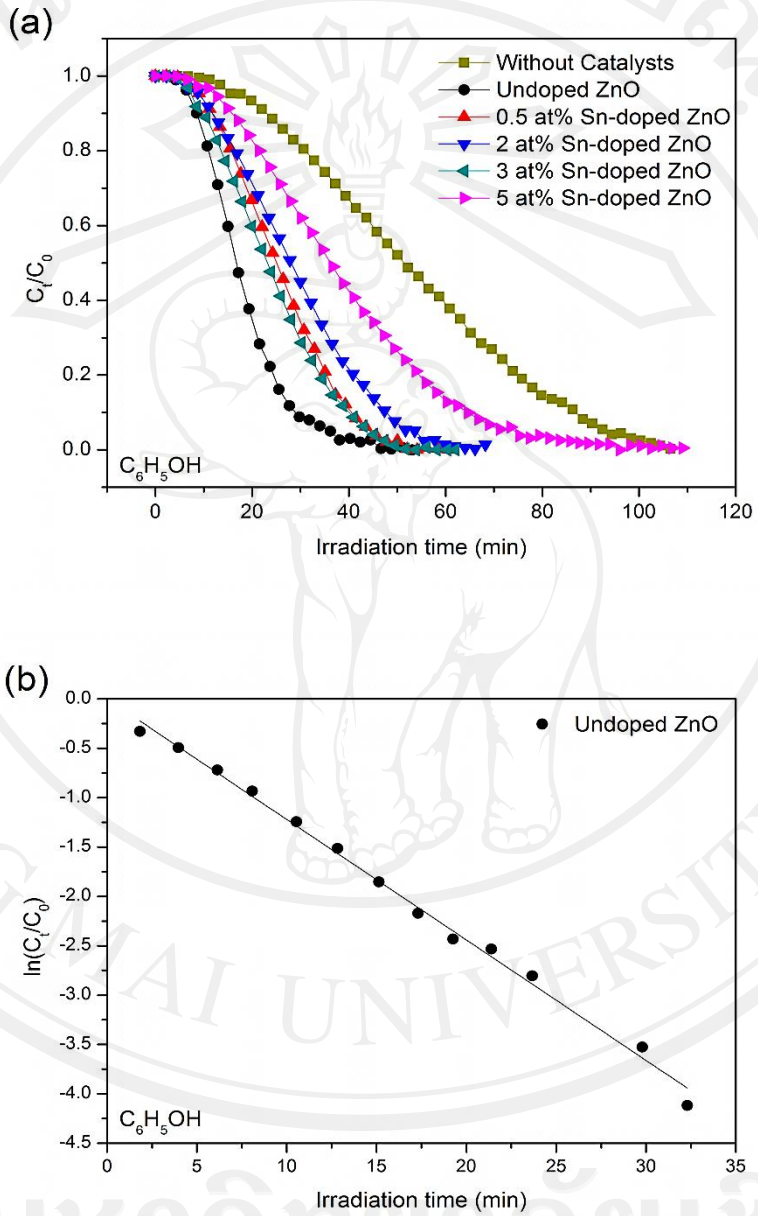

Figure 4.15 Photodegradation of C_6H_5OH with initial concentration (C_0) of 10 mg C/l over undoped and Sn-doped ZnO nanostructures under UVA irradiation: (a) change in C_6H_5OH concentration as a function of irradiation time, and (b) pseudo first-order degradation rate constant of undoped ZnO

ลิขสิทธิ์มหาวิทยาลัยเชียงใหม่
Copyright© by Chiang Mai University
All rights reserved

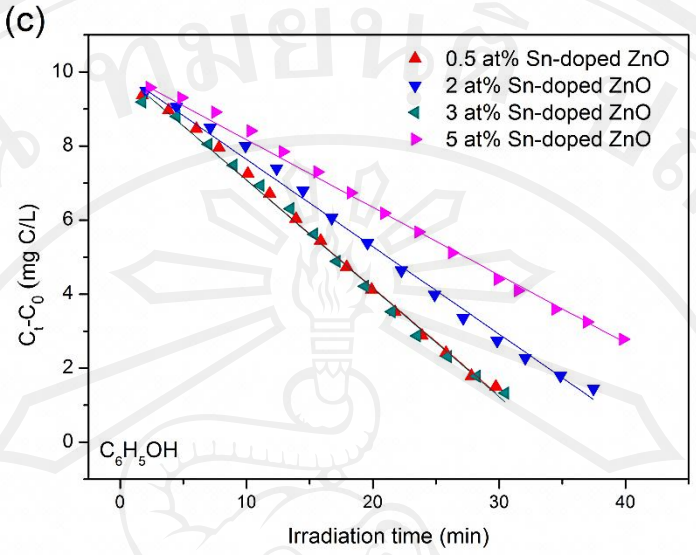

Figure 4.15 (cont.) Photodegradation of C_6H_5OH with initial concentration (C_0) of 10 mg C/l over undoped and Sn-doped ZnO nanostructures under UVA irradiation: (c) pseudo zero-order degradation rate constant of Sn-doped ZnO

By plotting $\ln(C_t / C_0)$, C_0 is initial organic concentration, versus irradiation time (Figure 4.15(b)), C_6H_5OH degradation over undoped ZnO was found to fit reasonably well with first-order kinetics as evidenced by high correlation coefficient value (R^2) of 0.9985. The apparent rate constant obtained in this case was 0.1220 min^{-1}. The result was consistent with that of Shukla et al. [182] in which C_6H_5OH photodegradation over ZnO under UV illumination followed first order kinetic scheme. However, in the case of Sn-doped ZnO samples, the photodegradation kinetics of C_6H_5OH was found to be zero-order at the beginning of the reaction as evidenced by good linear regression showing in Figure 4.15(c). The apparent zero-order rate constants of C_6H_5OH degradation over all Sn-doped samples are also presented in Table 4.1. By considering the calculated apparent rate constants obtained

ลิขสิทธิ์มหาวิทยาลัยเชียงใหม่
Copyright© by Chiang Mai University
All rights reserved

from undoped ZnO and Sn-doped ZnO catalysts, it is clearly seen that C_6H_5OH degradation over ZnO nanostructures process was faster than those over Sn-doped samples. The reason why Sn doping in ZnO gave a slower rate of C_6H_5OH photodegradation than that over undoped ZnO was possibly due to an electron-hole recombination inducement from the deep doping effect as a consequence of the deep state formation in ZnO bandgap energy [171, 183]. Upon doping Sn in ZnO structure via FSP process, Sn^{4+} ions could easily substitute into the Zn^{2+} site due to the similarity in their ionic radii [179]. Our results were consistent with the work by Carp et al. [129]. There in, the n-type dopants act as donor centers and favor the electron-hole recombination process, which is detrimental for the photoefficiency. Although, doping ZnO with Sn could increase surface area of the sample as evidenced from BET analysis, but the C_6H_5OH degradation activity of ZnO nanostructures was not improved in this study.

Table 4.1 The apparent zero-order rate constants of C_6H_5OH degradation over Sn-doped samples

Catalysts	**Zero-order rate kinetic expression:** $[C_t]=[C_0]-kt$	**Apparent zero-order rate constant ((mg C/l) . min^{-1})**	R^2
0.5 at% Sn-doped ZnO	10-0.2913t	0.2913	0.9994
2 at% Sn-doped ZnO	10-0.2360t	0.2360	0.9989
3 at% Sn-doped ZnO	10-0.2925t	0.2925	0.9991
5 at% Sn-doped ZnO	10-0.1828t	0.1828	0.9994

ลิขสิทธิ์มหาวิทยาลัยเชียงใหม่
Copyright© by Chiang Mai University
All rights reserved

Figure 4.16 shows the methanol (CH_3OH) photodegradation of undoped ZnO and Sn-doped ZnO catalysts under UVA irradiation. In the case of CH_3OH photodegradation under UVA irradiation, Sn-doped ZnO photocatalyst still exhibited the blocking results of the reaction rate of CH_3OH photodegradation using undoped ZnO. It was expected to the same cause of the C_6H_5OH photodegradation using Sn-doped ZnO being a photocatalyst. However, in the CH_3OH photodegradation process using a catalyst like ZnO, CH_3OH has a high density of C-H bonds which in turns reply on holes rather than $OH^{\bullet}$ radicals for their scission as suggested by Chen et al. [184−185] that degradation of CH_3OH took place by direct holes transfer at metal oxide surface, which contradict with the C_6H_5OH photodegradation taking place through successive insertion of $OH^{\bullet}$ radicals [129]. In terms of oxidizing power, both surface bound and free $OH^{\bullet}$ are known to possess very high oxidation potential which is only slightly lower compared to the VB potential. Therefore, the CH_3OH photodegradation naturally takes the time in the process longer than the C_6H_5OH photodegradation. The C_6H_5OH and CH_3OH photodegradation steps were explained in References [186] and [132], respectively. Thus, Figure 4.16 clearly showed the rate on the degradation of CH_3OH which is rather critically slower than that of C_6H_5OH in the case of both of undoped ZnO and Sn-doped ZnO as catalysts.

ลิขสิทธิ์มหาวิทยาลัยเชียงใหม่
Copyright© by Chiang Mai University
All rights reserved

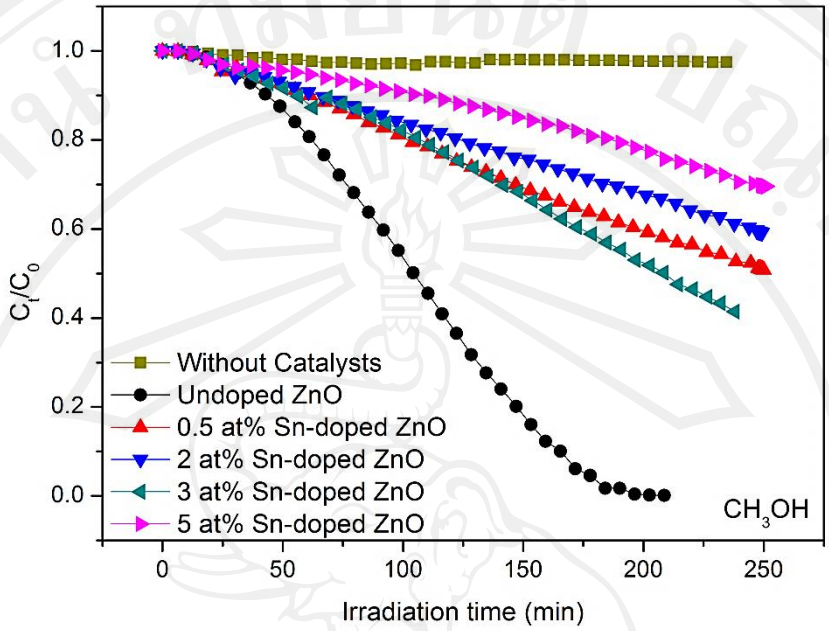

Figure 4.16 Change in CH_3OH concentration as a function of irradiation time on photodegradation of CH_3OH with initial concentration (C_0) of 500 μg C over undoped and Sn-doped ZnO nanostructures under UVA irradiation

ลิขสิทธิ์มหาวิทยาลัยเชียงใหม่
Copyright© by Chiang Mai University
All rights reserved